



Article

Effect of Sintering Temperature on the Properties of CuAlO_2 Synthesized from Nanosized Precursors for Application in Smart Infrastructure Systems

Shabnam Ghotbi ^{1,*}, Mohammad Abbas Mousa ², Lateef Najeh Assi ³  and SeyedAli Ghahari ⁴ 

¹ Birck Nanotechnology Center, Purdue University, West Lafayette, IN 47907, USA

² School of Civil Engineering, Engineering Campus, Universiti Sains Malaysia, Gelugor 11800, Penang, Malaysia; moh.mousa@student.usm.my

³ Department of Civil Engineering, Mazaya University College, Nasiriyah 64001, Iraq; lassi@email.sc.edu

⁴ Department of Civil and Environmental Engineering, Purdue University, West Lafayette, IN 47907, USA; sghahari@purdue.edu

* Correspondence: sghotbi@purdue.edu

Abstract: The current study aimed to evaluate the influence of different sintering temperatures on the properties of copper aluminum oxide (CuAlO_2) pellets synthesized from copper oxide (CuO) and aluminum hydroxide ($\text{Al}(\text{OH})_3$) for application in smart infrastructure systems. The pellets were sintered at 400 K, 1000 K, and 1300 K, in the presence of nitrogen gas flow to reduce the amount of oxygen availability. The CuAlO_2 sintered nanoparticles were chemically analyzed by X-ray diffractometry, and the nanostructure of the materials was studied by scanning electron microscopy. The transmittance of the sintered materials was examined by ultraviolet/visible (UV/Vis) spectrophotometry, and 88% transparency was observed for the pellets sintered at 1300 K. Electrical conductivity was measured at 0.905 mS/cm, indicating a semiconducting behavior.

Keywords: copper aluminum oxide; sintering; electrical conductivity; activation energy



Citation: Ghotbi, S.; Mousa, M.A.; Assi, L.N.; Ghahari, S. Effect of Sintering Temperature on the Properties of CuAlO_2 Synthesized from Nanosized Precursors for Application in Smart Infrastructure Systems. *Infrastructures* **2022**, *7*, 97. <https://doi.org/10.3390/infrastructures7070097>

Academic Editor: Pedro Arias-Sánchez

Received: 30 May 2022

Accepted: 8 July 2022

Published: 20 July 2022

Publisher's Note: MDPI stays neutral with regard to jurisdictional claims in published maps and institutional affiliations.



Copyright: © 2022 by the authors. Licensee MDPI, Basel, Switzerland. This article is an open access article distributed under the terms and conditions of the Creative Commons Attribution (CC BY) license (<https://creativecommons.org/licenses/by/4.0/>).

1. Study Background

Thermoelectric (TE) materials have attracted significant attention due to their ability to convert waste heat into electricity. As a heat engine, TE devices have many benefits, including no moving parts, silence, compactness, and ease of integration into the existing infrastructure [1,2]. In particular, fabricating a transparent TE device with transparent p–n junctions for electricity generation and ultraviolet (UV) absorbance in smart infrastructure systems is a promising idea. Kawazoe et al. stated that CuAlO_2 (CAO), a transparent and conductive p-type material, has good potential for TE applications [3]. The most prominent application for using transparent TE devices is in the construction industry, where UV-absorbing windows are required. CAO is a wide-bandgap material that can absorb UV light and transmit visible light [4]. Zheng et al. showed that CAO has the ability of ozone sensing, and it can form transparent p–n junction ozone sensors with existing n-type transparent materials such as In_2O_3 [5]. In conjunction with a well-known transparent n-type semiconductor such as ZnO or SnO_2 [6,7], these devices have a wide range of uses varying from flat-panel displays to transparent solar cells. These p–n junctions would allow solar cells to be placed on pre-existing windows, allowing most optical light to pass and generating electricity through the absorption of UV rays [8,9]. Studies have shown that, by using thin films of CAO coupled with an n-type semiconductor such as ZnO, promising thermoelectric results can be achieved while maintaining optical transparency [10,11].

CAO thin films can be fabricated through several techniques. The current processes for creating CAO are energy-inefficient, which yields poor outcomes. Promising results for the synthesis of CAO have been delivered using many different techniques such as

hydrothermal synthesis, direct microwaving of precursors, mixing precursors in a bath of molten NaOH, or a high-temperature solid-state reaction [12–15]. Neumann-Spallart et al. deposited CAO by pulsed laser deposition (PLD), resulting in $0.3 \text{ S}\cdot\text{cm}^{-1}$ conductivity with a 280 nm thick film made of sapphire [16]. The magnetron sputtering deposition technique led to an electrical resistivity of $0.24 \text{ S}\cdot\text{cm}^{-1}$ and a direct bandgap of 3.26 eV [17]. The same deposition technique resulted in a Seebeck coefficient of $230 \mu\text{V}\cdot\text{K}^{-1}$ [18]. Ren et al. deposited CAO on quartz substrates via a sol–gel process and obtained 79% transmittance at 780 nm [19]. Gong et al. achieved a significantly high room-temperature conductivity of $2 \text{ S}\cdot\text{cm}^{-1}$ and $1.8 \times 10^{19} \text{ cm}^{-3}$ carrier concentration using the chemical vapor deposition technique [20].

Before integrating TE devices, nanosized powders, as well as bulk materials of CAO, need to be synthesized. Sato et al. synthesized CAO crystals at 400°C with a titanium alloy autoclave [21]. The parameters such as molar ratio and pH of the materials, hydrothermal temperature and pressure, and reaction time were found to have a significant effect on the crystal formation and morphologies [22–24]; in another experiment, 80 nm CAO powders were synthesized for application in ozone sensing with a hydrothermal process at 250°C [25]. However, to reach an improved crystallinity, annealing at high temperatures over 1100°C is needed. In another study performed by Dloczik et al., CAO powders were obtained via $\alpha\text{-LiAlO}_2$ ion exchange with CuCl at 800 K [26]. Ingram et al. synthesized CAO from $\text{Cu}_2\text{O}/\text{CuO}$ and Al_2O_3 in molten NaOH solution at 360°C [12]. In this research, the hydrothermal process increased the hole concentration compared with the solid-state process, according to which the electrical conductivity differed [12]. In hydrothermal synthesis, precursor quality, pH solution, and the atmosphere inside the oven must be perfectly set up and monitored to have a significant CAO yield [27]. Due to this extraordinary challenge, hydrothermal synthesis of CAO is not easily scalable, and it is not a feasible option for commercialization or further studies of the CAO properties. Although a comparatively low reaction temperature is the advantage of the hydrothermal synthesis, microscale CAO powders obtained in this process lead to a lower performance of the junction [23,28]. Therefore, an unconventional solid-state synthesis of CAO is required if nanoscale powders are the ultimate goal for fabrication. To have atomic-level mixing, the sintering process should take place in an inert atmosphere, especially if the sol–gel method of fabrication is followed. For instance, in the presence of argon, pure CAO can be obtained in 4 h using a nitrate-based metal ion in an inorganic/polymer double-gel process. Alternatively, under an oxygen partial pressure $p(\text{O}_2)$ of 10^{-5} atm, CAO can be synthesized after 48 h [29].

2. Research Importance

Most conventional solid-state reactions require temperatures above 1200 K and several hours of furnace exposure [30,31]. Such high temperatures can be reduced significantly through several techniques. Yu et al. performed the synthesis of CAO and proved that the reaction could be completed at 1000 K using thin films of precursors applied onto silicon and quartz wafers; in this research study, as the annealing temperature increased from 1000 K to 1100 K, there was a substantial increase in the grain size [4]. At temperatures below 700 K, CAO is unstable thermodynamically in the air, and, if the temperature goes below 700 K, the instability of CuAlO_2 causes the formation of Cu^{2+} cations in the CuAl_2O_4 phase [32]. Therefore, reactions for the solid-state approach are required to take place at temperatures over 1000 K for about 100 h [27,33,34]; however, the reaction time can be significantly reduced if the precursors are put in a furnace with argon gas. Mudena et al. reduced the calcination time to 1.5 h in an argon atmosphere and synthesized a highly polycrystalline and pure delafossite phase of CAO [35]. In another study, CAO was synthesized for 2 h in the presence of air. In this study, copper(I) acetate loaded with boehmite nanorods was used as a precursor [36]. In a similar approach, CAO ceramic was synthesized by nano boehmite and Cu_2O as precursors for 2 h in an argon atmosphere [37].

Achieving a homogeneous mixture of the precursors while maintaining a comparatively low heat temperature is necessary for the synthesis of a highly crystalline, single-phase CAO. To the best of our knowledge, the effect of different ratios of the precursors required for CAO synthesis, i.e., CuO and Al(OH)₃, on the performance and thermal properties of this p-type material has not been studied. Herein, this paper aimed to improve the characteristics of CAO synthesized under different annealing temperatures. This research project used a single-step firing process to synthesize CAO. We obtained a well-dispersed slurry with ball milling; vacuum filtration casting was used to separate the solid and liquid phases, and the solid phase was dried and pelletized. Then, annealing was performed under nitrogen gas flow at 400 K, 1000 K, and 1300 K to synthesize bulk CAO. Moreover, the electrical and transparency properties of the synthesized CAO were measured, and the microstructure was studied with SEM and XRD analysis.

3. Methodology

In this work, nano powders were obtained from Sigma-Aldrich. The physical and chemical characteristics of CuO powder with a shiny black color appearance and Al(OH)₃ powder with a rock salt appearance were as follows: The CuO and Al(OH)₃ molar masses were 79.55 g/mol and 78.00 g/mol, respectively. The CuO and Al(OH)₃ average particle sizes were 50 nm and 30 nm. The X-ray diffraction (XRD) analysis of CuO is presented in Figure 1. All the peaks shown in Figure 1 are associated with the monoclinic phase of CuO. The phase is related to the Joint Committee on Powder Diffraction Standards (JCPDS) file card no. 48-1548 Tenorite indicates the fact that the obtained slurry was a single phase. The precursors were mixed in a 1:1 ratio with a ball milling machine as the grinding medium. A total of 20 g of powders were mixed with deionized water, and 4 mL of polyethylene glycol with an average molar weight of 200 and a viscosity of 4.3 c St. The ball milling process was performed for 8 h. The obtained slurry from the ball milling process was cast on a glass substrate and kept at 296 K for 5 h. The cast mixtures were then heated in an oven at 400 K for 24 h until a dark-gray specimen was observed. A uniaxial dry press was used to form the pellets. At 160 MPa pressure, the pieces of the dried specimen were compacted, and a 1.5 mm × 15 mm cylindrical shape pellet was formed. After this stage, the pellets were sintered in a tube furnace and kept in the presence of flowing nitrogen gas at 400 K, 1000 K, and 1300 K for 5 h to study the effect of different annealing temperatures on the composition of sintered samples.

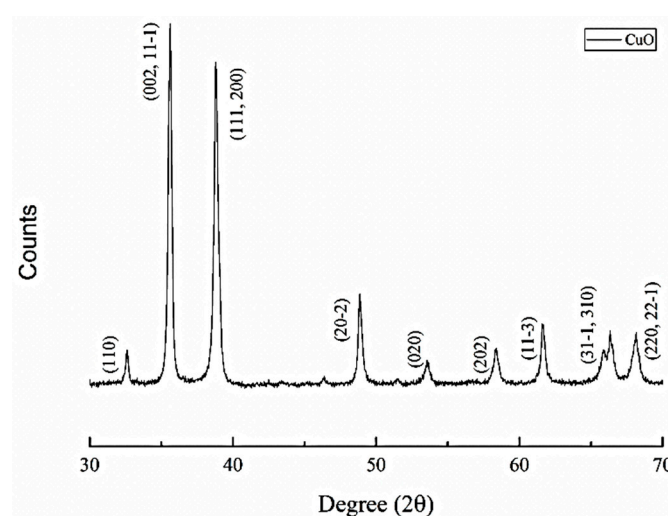


Figure 1. XRD analysis of CuO.

4. Characterization

Phase characterization and crystalline composition quantification were carried out through X-ray diffraction (XRD) analysis. The samples were crushed and powered for XRD analysis with Siemens D500. The powder was situated in Cu K α radiation and Ni filter with 50 kV and 30 mA working conditions for 30°–70° (2 θ) range analysis with a step size of 0.02°. Jade software was used to analyze the results. Samples were tested in a titanium cylinder containing nitrogen gas with a scanning rate of 10 °C/min from 25 °C to 1000 °C. Field-emission scanning electron microscopy (FE-SEM) using FEI Quanta 3D FEG was performed to study the microstructure of the precursors and the fractured surface of the sintered samples. To prepare CuO nanopowders for SEM micrography, the particles were sonicated for 60 min in polyvinylpyrrolidone (PVP) and water, and the obtained liquid was placed on a cleaned glass film and dried at the room temperature.

To determine the optical properties of the sintered material, ultraviolet/visible (UV/Vis) spectrophotometry with an Agilent Cary 600i UV/Vis/near-IR spectrophotometer was used in the range of 300 to 1000 nm. At 60 nm/min with a 2 nm interval scan rate, the spectra were collected from the samples in a standard quartz cuvette and analyzed. Then, 0.020 g of CAO powder from the ground sintered pellets was dispersed in 50 mL of DI water and sonicated for 60 min. Next, 10 mL of this aqueous solution was diluted in 30 mL of DI water. Prior to testing, to improve the gas sorption kinetics, ground sintered pellets of CAO were put in a vacuum chamber at 80 °C for 12 h. The two-probe technique was implemented to determine the electrical properties of the pellets. Keithley's nanovoltmeter (2182A) paired with Keithley's current source (6221) was used to measure resistivity under different temperatures ranging from 25 °C to 100 °C.

5. Results

The slurry was kept at 296 K for 5 h, and the precursors were ball-milled in the presence of water and polyethylene glycol (PEG 200) for 12 h. The cast mixtures were heated in an oven at 400 K for 24 h. Next, 8 g of the specimen was heat-treated at 1000 K and 1300 K for further experiments. Then, 1.2 g of the cracked specimens were first pressed under 160 MPa into a 15 mm diameter mold and were subsequently heat-treated at 1000 K and 1300 K. The thickness of all pellets was kept at 1 mm. The CAO ceramics were obtained by sintering the pellets and the cracked parts in a tube furnace in the presence of nitrogen gas at 1000 K and 1300 K for 5 h. The CAO pellet in gray color is shown in Figure 2. XRD analysis was performed on the pellets sintered at different temperatures to study the phase composition of CAO. The patterns shown in Figure 3 are in decreasing order in terms of the sintering temperature. According to Figure 3, the CAO phase in the pellet sintered at 1300 K was higher than that of the other pellets. The peaks associated with 42°, 51°, 76°, and 92° were the main peaks related to the composition of CAO; the XRD results showed that, at lower temperatures, the amount of CAO was considerably lower than that at higher temperatures. The pattern at the bottom refers to the specimen sintered at 400 K, which illustrates that the reactions did not lead to a highly pure CAO, when exposed to the temperature for 5 h. The pattern related to the sample sintered at 1000 K indicated the formation of phases other than the CAO composition. For the pellets sintered at 1000 K, a secondary phase containing Cu₂O peak was observed, and the peaks related to CAO in this pattern were considerably higher than those of the lower pattern. At 38°, 40°, and 62°, the composition of Cu₂O was illustrated. The presence of Cu₂O could have been due to the low amount of oxygen while sintering; CuO goes through a decomposition reaction in which Cu²⁺ ions reduce to Cu⁺, and the products of this reaction are Cu₂O(s) and O₂(g). It has been proven that Cu₂O can be formed from CuO crystallites at 1100–1200 K in the presence of nitrogen [38] and argon gas [39].



Figure 2. The fabricated sintered CAO pellet.

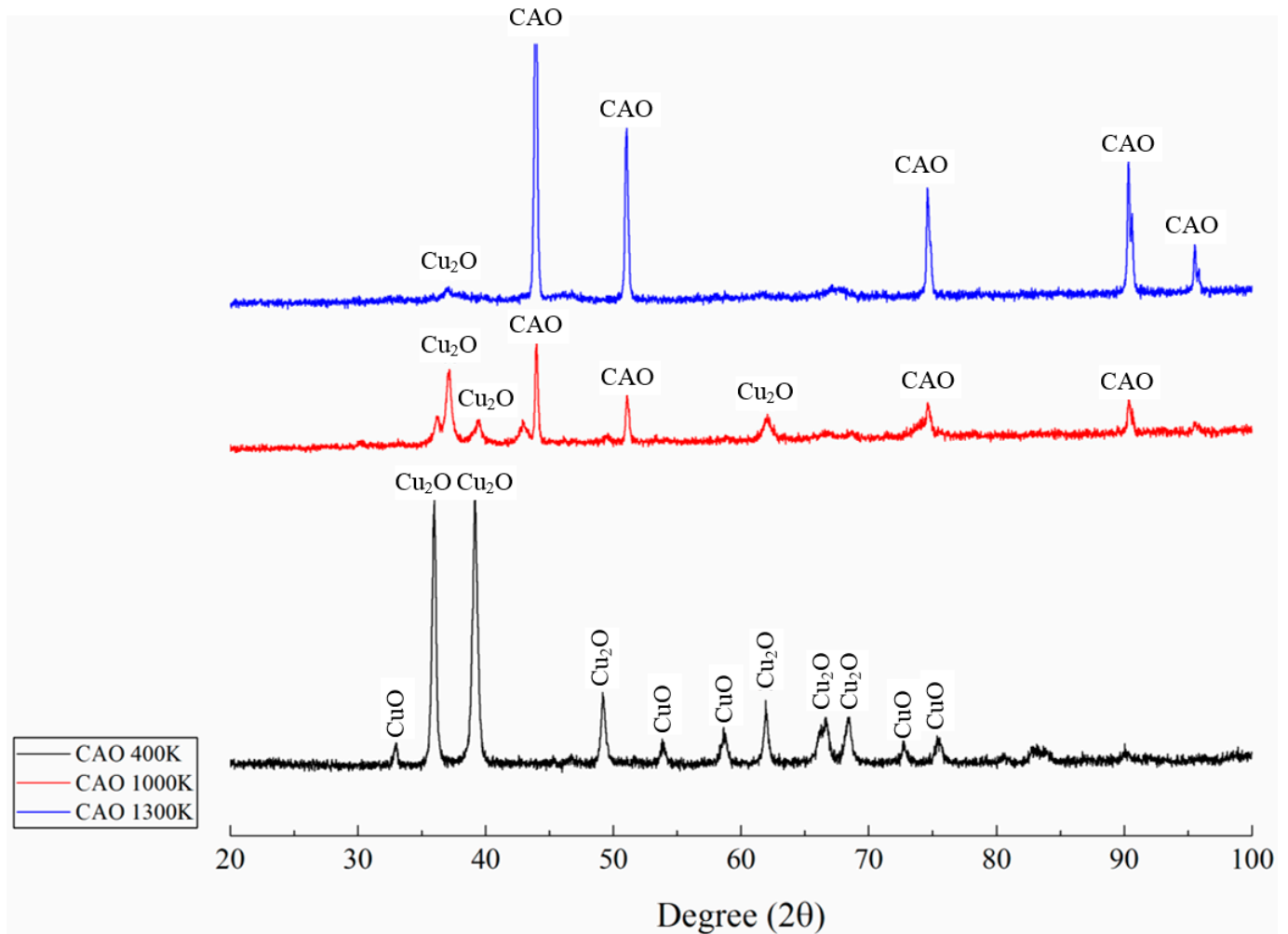


Figure 3. XRD analysis of CAO pellets sintered at 400 K, 1000 K, and 1300 K under flowing nitrogen gas for 5 h.

In XRD and crystallography, the size of sub-micrometer particles or crystallites can be related to each other via the Scherrer equation. The size of crystal powders can be determined using the Scherrer equation as follows:

$$\tau = \frac{K\lambda}{\beta \cos(\theta)}, \quad (1)$$

where τ is the mean size of the crystalline domains, K is the shape factor (typically about 1 for spherical particles), λ is the X-ray wavelength, β is the line broadening at half of the maximum intensity, and θ is the Bragg angle. In this study, the peak at 35.78 °C was chosen to calculate the crystallite size, and the corresponding average size was 55 nm. The results fell between the ranges of the average crystallite size reported in the literature [29,39].

FE-SEM images were obtained from the fractured surface of the sintered CAO pellets to study the microstructure and morphology of the specimens. According to the micrograph presented in Figure 4b, for the specimen sintered at the lower temperature, the shape of the grains was irregular, and the pockets were not firmly connected to each other; the typical shape of the grains was elongated and plate-shaped. Figure 4a, however, illustrates spherical, regular-shaped pockets representing the CAO compositions; a higher magnification of Figure 4a can be seen in Figure 5, confirming the above statement. CAO contains layers of Cu and AlO₂ composition, which consists of AlO₆ [40]. Therefore, the conductivity is higher in value when it is measured parallel to the layers due to the metal bonding between the Cu atoms [41]. However, this anisotropy could be disregarded while analyzing the data since the grains orient randomly [42]. CuO reacts with Al(OH)₃ according to the following reaction, and the resulting molar mass of Cu(OH)₂, Al, and O is 97.56 g/mol, 26.98 g/mol, and 15.99 g/mol, respectively.

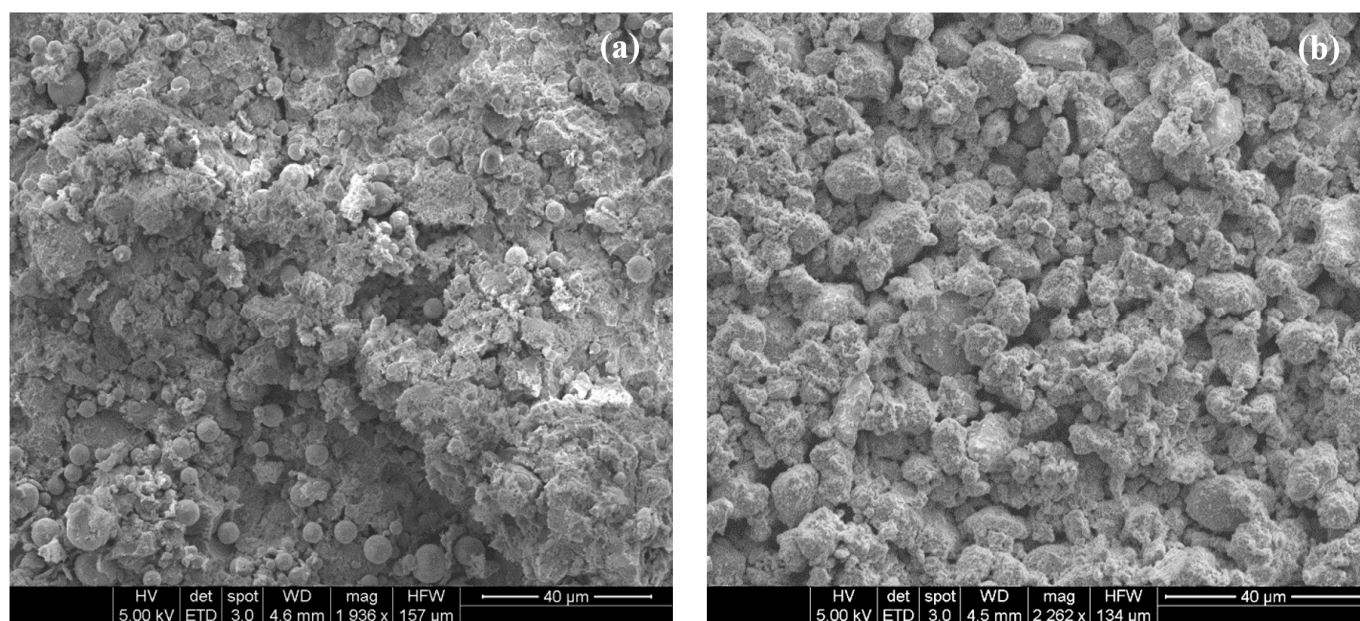
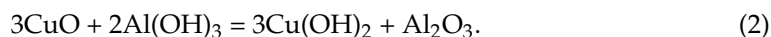


Figure 4. SEM images of all CAO pellets sintered at (a) 1300 K and (b) 1000 K.

UV/Vis spectrometry in the wavelength of 300–1000 nm was used to study the optical properties of the specimens. The spectrometry results of the sintered CAO particles prepared in an aqueous suspension form are illustrated in Figure 6. The maximum transmittance for the sample sintered at 1300 K was 88% at 1000 nm wavelength, which is similar to the values reported elsewhere [8,43]. According to the results obtained from UV/Vis spectrometry illustrated in Figure 6, the transmittance of the sample sintered at 1000 K increased with a lower wavelength. The increase in the transparency at the wavelength of 300–360 nm could be due to the irregular shape of the grains and the pockets not being firmly connected to each other. The CAO sample sintered at 1300 K showed a similar pattern to that sintered at 1000 K; however, the increase in the transparency occurred at a lower wavelength, conforming to the results reported elsewhere [8]. The optical bandgap of

semiconductor materials can be calculated through the electron excitation from the valence band to the conduction band. The bandgap can be obtained from the following equation:

$$(\alpha h\nu)^n = A(h\nu - E_g), \quad (3)$$

where α is the optical absorption coefficient, $h\nu$ is the photon energy, $n = 2$ for direct band transition, A is a constant, and E_g is the optical bandgap. The direct bandgap of the specimen sintered at 1300 K was calculated at 2.90 eV, whereas this value was calculated at 2.7 eV for the specimen sintered at 1000 K, conforming to the results reported elsewhere [44,45].

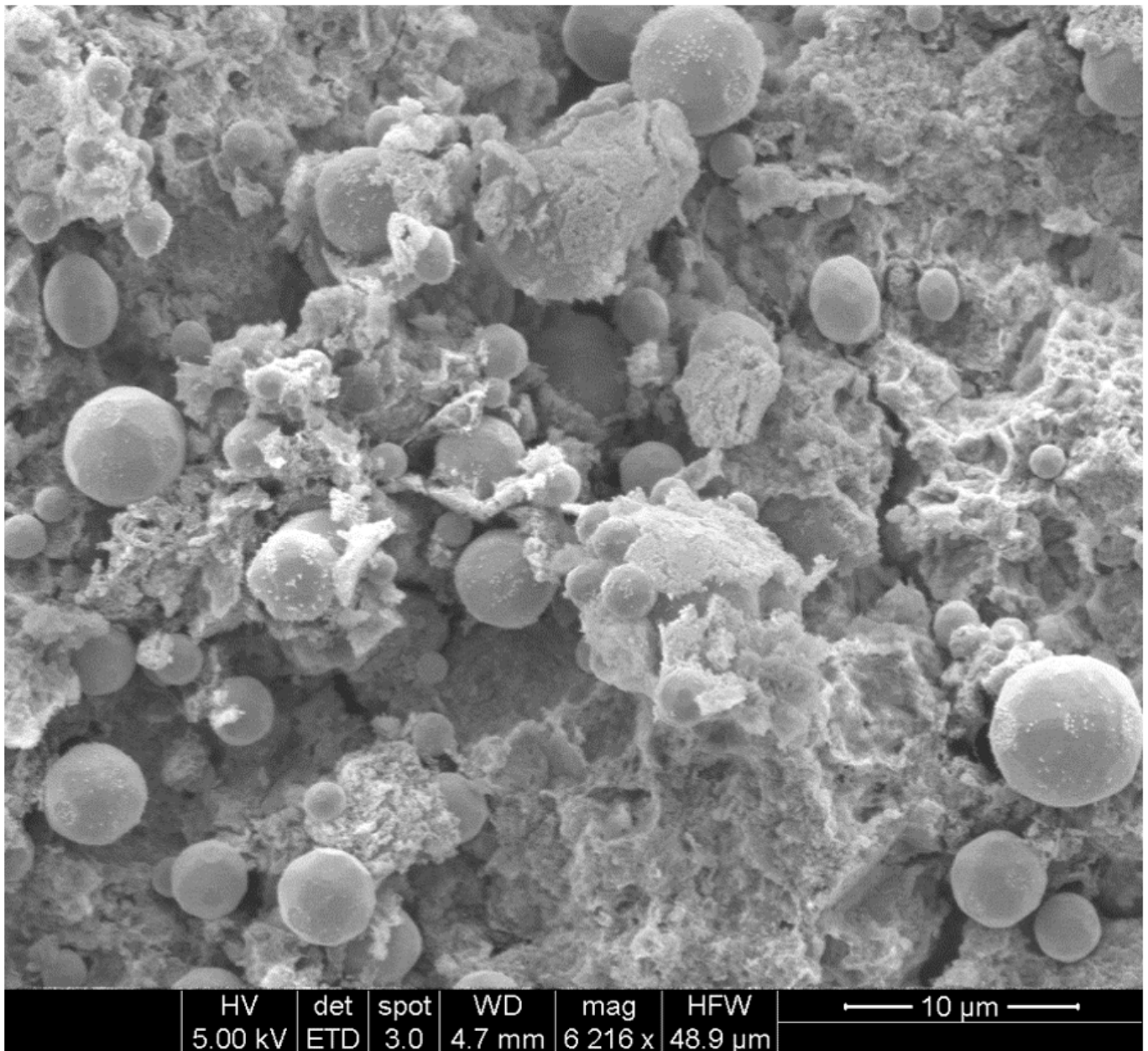


Figure 5. CAO sample sintered at 1300 K. Spherical, regular-shaped pockets associated with the composition of CAO.

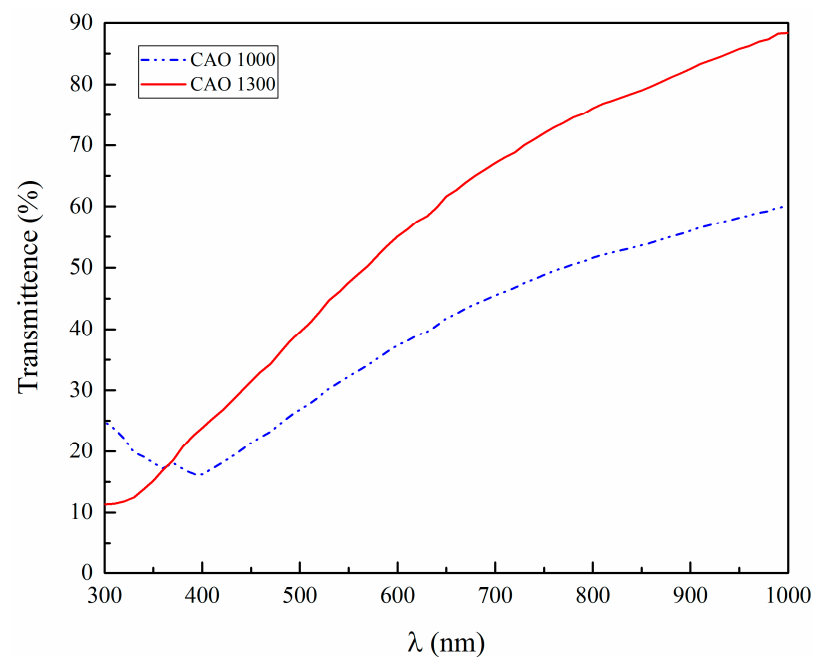


Figure 6. The transmittance of CAO nanoparticles sintered at different temperatures.

Two-probe measurement techniques were implemented to assess the CAO pellets' electrical properties. The temperature range was set from 313 to 373 K, and the test results of the electrical conductivity of CAO pellets sintered at different temperatures are illustrated in Figure 7. As shown, when the temperature increased, the conductivity of the samples increased. It can be concluded from the two-probe measurement that a higher sintering temperature could lead to a higher electrical conductivity. The CAO pellet sintered at 1300 K showed a 19.7% increase in the conductivity measurements at its highest value compared with that of the CAO pellet sintered at 1000 K. The highest value of the electrical conductivity of the sample sintered at 1000 K was 0.756 mS/cm, which could be due to the fact that, at lower temperatures, the porosity of the sample is comparatively high; however, a mercury intrusion porosimetry test is required to prove this statement [46].

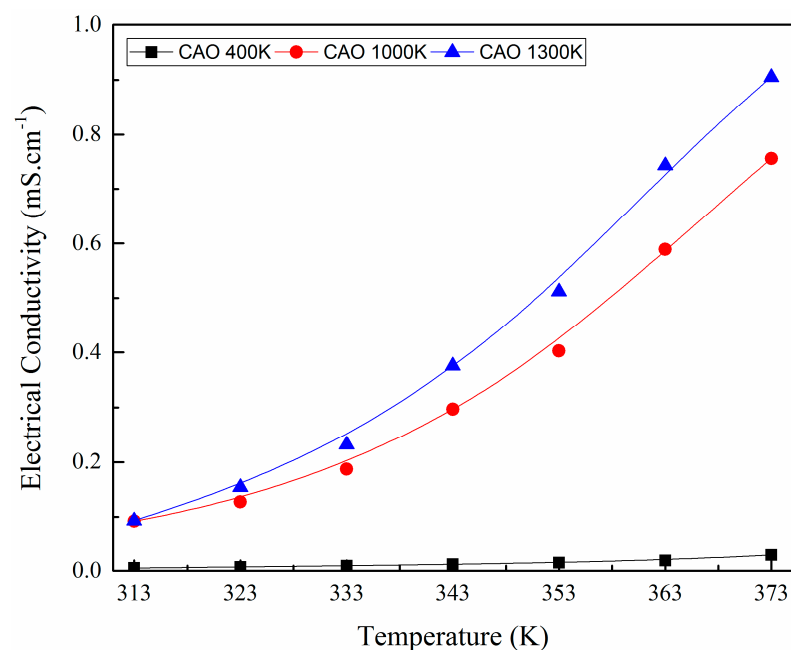


Figure 7. Electrical conductivity of CAO pellets sintered at 400 K, 1000 K, and 1300 K.

Benko and Koffyberg proved that the random orientation of the grains has a negative effect on the conductivity [42]; in addition, Lee et al. showed that, because of the structural anisotropy of the CAO crystals, the electrical conductivity along the ab plane was higher than that of the c axis. CAO contains O–Cu–O layers in line with the c axis, i.e., AlO_6 layers; furthermore, Cu layers, known as the conduction paths, are situated in the ab plane, i.e., perpendicular to the c axis [47]. According to a research study performed by Ishiguro et al., the distance between the two atoms of Cu was estimated at 2.86 Å, longer than that of a metallic copper, i.e., 2.56 Å. This indicates that the nonbonding orbitals of Cu^+ ions are responsible for the semi-conduction band in the layers perpendicular to the c axis [40]. Although the acquired electrical conductivity was in agreement with the reported conductivities reported elsewhere [35,45], a considerably low conductivity of 0.15 mS/cm was reported for the sol–gel process [39].

6. Conclusions

This paper aimed to improve the characteristics of CAO synthesized under different sintering temperatures and with different precursor ratios. This research project used a single-step firing process to synthesize CAO. The precursor nanoparticles were pressed and annealed under nitrogen gas flow at 400 K, 1000 K, and 1300 K to synthesize bulk CAO. The highest value of the electrical conductivity of the sample sintered at 1000 K was 0.756 mS/cm, and the results indicate that the CAO pellet sintered at 1300 K showed a 19.7% increase in the conductivity measurements at its highest value. Higher sintering temperatures led to a dense crystalline structure. The maximum transmittance for the sample sintered at 1300 K was measured to be 88% at 1000 nm wavelength. On the basis of this research study, it can be concluded that sintering at 1300 K in the presence of nitrogen gas flow could be a promising fabrication method for delafossite-type oxides. By implementing such a method, nanosized, high-surface-area materials can be fabricated, which could be used as the p-leg in thermoelectric devices for smart infrastructure systems.

Author Contributions: Data curation, S.G. (Shabnam Ghotbi) and S.G. (Seyedali Ghahari); formal analysis, S.G. (Shabnam Ghotbi) and M.A.M.; investigation, M.A.M., L.N.A. and S.G. (Seyedali Ghahari); methodology, S.G. (Shabnam Ghotbi), M.A.M. and L.N.A.; validation, S.G. (Shabnam Ghotbi), M.A.M. and S.G. (Seyedali Ghahari); visualization, S.G. (Shabnam Ghotbi) and S.G. (Seyedali Ghahari); writing—original draft, M.A.M. and S.G. (Seyedali Ghahari); writing—review and editing, S.G. (Shabnam Ghotbi). All authors have read and agreed to the published version of the manuscript.

Funding: This research received no external funding.

Institutional Review Board Statement: Not applicable.

Informed Consent Statement: Not applicable.

Data Availability Statement: The datasets used in this study are available from the corresponding author.

Conflicts of Interest: The authors declare no conflict of interest.

References

1. Nolas, G.S.; Sharp, J.; Goldsmid, J. *Thermoelectrics: Basic Principles and New Materials Developments*; Springer Science & Business Media: Berlin/Heidelberg, Germany, 2013; Volume 45.
2. Ghahari, S. *The Effect of ZnO nanoparticles on Thermoelectric Behavior and Fresh Properties of Cement Paste*; Purdue University: City of West Lafayette, IN, USA, 2016.
3. Kawazoe, H.; Yasukawa, M.; Hyodo, H.; Kurita, M.; Yanagi, H.; Hosono, H. P-type electrical conduction in transparent thin films of CuAlO_2 . *Nature* **1997**, *389*, 939–942. [[CrossRef](#)]
4. Yu, R.S.; Lu, C.J.; Tasi, D.C.; Liang, S.C.; Shieu, F.S. Phase transformation and optoelectronic properties of p-type CuAlO_2 thin films. *J. Electrochem. Soc.* **2007**, *154*, H838–H843. [[CrossRef](#)]
5. Zheng, X.G.; Taniguchi, K.; Takahashi, A.; Liu, Y.; Xu, C.N. Room temperature sensing of ozone by transparent p-type semiconductor CuAlO_2 . *Appl. Phys. Lett.* **2004**, *85*, 1728–1729. [[CrossRef](#)]
6. Min, H.; Lee, D.Y.; Kim, J.; Kim, G.; Lee, K.S.; Kim, J.; Paik, M.J.; Kim, Y.K.; Kim, K.S.; Kim, M.G. Perovskite solar cells with atomically coherent interlayers on SnO_2 electrodes. *Nature* **2021**, *598*, 444–450. [[CrossRef](#)]

7. Xiong, L.; Guo, Y.; Wen, J.; Liu, H.; Yang, G.; Qin, P.; Fang, G. Review on the application of SnO₂ in perovskite solar cells. *Adv. Funct. Mater.* **2018**, *28*, 1802757. [\[CrossRef\]](#)
8. Akyildiz, H. Synthesis of CuAlO₂ from chemically precipitated nano-sized precursors. *Ceram. Int.* **2015**, *41*, 14108–14115. [\[CrossRef\]](#)
9. Pedapudi, M.C.; Dhar, J.C. Ultrasensitive pn Junction UV-C Photodetector Based on p-Si/ β -Ga₂O₃ Nanowire Arrays. *Sens. Actuators A Phys.* **2022**, *344*, 113673. [\[CrossRef\]](#)
10. Pan, J.; Sheng, Y.; Zhang, J.; Huang, P.; Zhang, X.; Feng, B. Photovoltaic Conversion Enhancement of a Carbon Quantum Dots/p-Type CuAlO₂/n-Type ZnO Photoelectric Device. *ACS Appl. Mater. Interfaces* **2015**, *7*, 7878. [\[CrossRef\]](#) [\[PubMed\]](#)
11. Urper, O.; Baydogan, N. Effect of Al concentration on optical parameters of ZnO thin film derived by Sol-Gel dip coating technique. *Mater. Lett.* **2020**, *274*, 128000. [\[CrossRef\]](#)
12. Ingram, B.; Gonzalez, G.B.; Mason, T. Transport and defect mechanisms in cuprous delafossites. 1. Comparison of hydrothermal and standard solid-state synthesis in CuAlO₂. *Chem. Mater.* **2004**, *16*, 5616–5622. [\[CrossRef\]](#)
13. Saha, B.; Thapa, R.; Chattopadhyay, K.K. A novel route for the low temperature synthesis of p-type transparent semiconducting CuAlO₂. *Mater. Lett.* **2009**, *63*, 394–396. [\[CrossRef\]](#)
14. Tong, B.; Deng, Z.; Meng, G.; Chang, J.; Lu, Y.; Qi, L.; Shan, X.; Shao, J.; Wang, S.; Shen, C. Ultrasensitive and selective CuAlO₂ sensor toward H₂S based on surface sulfuration-desulfuration reaction. *Sens. Actuators B Chem.* **2020**, *313*, 128027. [\[CrossRef\]](#)
15. Lee, T.-H.; Hwang, S.-M.; Yoo, M.-J. Investigation of CuAlO₂ composite dielectric properties and selective metallization by laser direct structure technology. *J. Eur. Ceram. Soc.* **2020**, *40*, 1390–1397. [\[CrossRef\]](#)
16. Neumann-Spallart, M.; Pai, S.P.; Pinto, R. PLD growth of CuAlO₂. *Thin Solid Film.* **2007**, *515*, 8641–8644. [\[CrossRef\]](#)
17. Yu, R.-S.; Yin, H.-H. Structural and optoelectronic properties of p-type semiconductor CuAlO₂ thin films. *Thin Solid Film.* **2012**, *526*, 103–108. [\[CrossRef\]](#)
18. Banerjee, A.N.; Maity, R.; Ghosh, P.K.; Chattopadhyay, K.K. Thermoelectric properties and electrical characteristics of sputter-deposited p-CuAlO₂ thin films. *Thin Solid Film.* **2005**, *474*, 261–266. [\[CrossRef\]](#)
19. Ren, Y.; Zhao, G.; Zhang, C.; Chen, Y. Preparation of CuAlO₂ thin films with high transparency and low resistivity using sol-gel method. *J. Sol-Gel Sci. Technol.* **2012**, *61*, 565–569. [\[CrossRef\]](#)
20. Gong, H.; Wang, Y.; Luo, Y. Nanocrystalline p-type transparent Cu–Al–O semiconductor prepared by chemical-vapor deposition with Cu(acac)₂ and Al(acac)₃ precursors. *Appl. Phys. Lett.* **2000**, *76*, 3959–3961. [\[CrossRef\]](#)
21. Sato, T.; Sue, K.; Tsumatori, H.; Suzuki, M.; Tanaka, S.; Kawai-Nakamura, A.; Saitoh, K.; Aida, K.; Hiaki, T. Hydrothermal synthesis of CuAlO₂ with the delafossite structure in supercritical water. *J. Supercrit. Fluids* **2008**, *46*, 173–177. [\[CrossRef\]](#)
22. Xiong, D.; Zeng, X.; Zhang, W.; Wang, H.; Zhao, X.; Chen, W.; Cheng, Y.-B. Synthesis and Characterization of CuAlO₂ and AgAlO₂ Delafossite Oxides through Low-Temperature Hydrothermal Methods. *Inorg. Chem.* **2014**, *53*, 4106–4116. [\[CrossRef\]](#)
23. Hao, L.; Zhang, Y.; Kubomura, R.; Ozeki, S.; Liu, S.; Yoshida, H.; Jin, Y.; Lu, Y. Preparation and thermoelectric properties of CuAlO₂ compacts by tape casting followed by SPS. *J. Alloys Compd.* **2021**, *853*, 157086. [\[CrossRef\]](#)
24. Ma, L.; Dong, C.; Li, W.; Su, Q.; Zhou, J.; Xie, E.; Lan, W. Room-temperature power factor of CuAlO₂ composite tablets enhanced by MWCNTs. *Curr. Appl. Phys.* **2022**, *33*, 27–32. [\[CrossRef\]](#)
25. Thirumalairajan, S.; Mastelaro, V.R.; Escanhoela, C.A. In-Depth Understanding of the Relation between CuAlO₂ Particle Size and Morphology for Ozone Gas Sensor Detection at a Nanoscale Level. *ACS Appl. Mater. Interfaces* **2014**, *6*, 21739–21749. [\[CrossRef\]](#)
26. Dloczik, L.; Tömm, Y.; Könenkamp, R.; Lux-Steiner, M.C.; Dittrich, T. CuAlO₂ prepared by ion exchange from LiAlO₂. *Thin Solid Film.* **2004**, *451–452*, 116–119. [\[CrossRef\]](#)
27. Kaya, I.; Cetin, C.; Aydin, H.; Katircioglu, Z.; Buyukbekar, B.; Yavuz, M.S.; Uyaner, M.; Kalem, V.; Akyildiz, H. Production of CuAlO₂ in powder, bulk and nanofiber forms. *J. Ceram. Process. Res.* **2015**, *16*, 648–655.
28. Chen, X.-L.; Zhang, J.-X.; Zhao, Z.-Y. First-principles calculations to investigate the polymorph effects of CuAlO₂. *Comput. Mater. Sci.* **2022**, *209*, 111403. [\[CrossRef\]](#)
29. Ahmed, J.; Blakely, C.K.; Prakash, J.; Bruno, S.R.; Yu, M.; Wu, Y.; Poltavets, V.V. Scalable synthesis of delafossite CuAlO₂ nanoparticles for p-type dye-sensitized solar cells applications. *J. Alloys Compd.* **2014**, *591*, 275–279. [\[CrossRef\]](#)
30. Ruttanapun, C.; Kosalwat, W.; Rudradawong, C.; Jindajitawat, P.; Buranasiri, P.; Naenkieng, D.; Boonyopakorn, N.; Harnwunggmoung, A.; Thowladda, W.; Neeyakorn, W.; et al. Reinvestigation Thermoelectric Properties of CuAlO₂. *Energy Procedia* **2014**, *56*, 65–71. [\[CrossRef\]](#)
31. Byrne, D.; Cowley, A.; McNally, P.; McGlynn, E. Delafossite CuAlO₂ film growth and conversion to Cu–Al₂O₃ metal ceramic composite via control of annealing atmospheres. *Crystengcomm* **2013**, *15*, 6144–6150. [\[CrossRef\]](#)
32. Kumekawa, Y.; Hirai, M.; Kobayashi, Y.; Endoh, S.; Oikawa, E.; Hashimoto, T. Evaluation of thermodynamic and kinetic stability of CuAlO₂ and CuGaO₂. *J. Therm. Anal. Calorim.* **2010**, *99*, 57–63. [\[CrossRef\]](#)
33. Amrute, A.P.; Łodziana, Z.; Mondelli, C.; Krumeich, F.; Pérez-Ramírez, J. Solid-State Chemistry of Cuprous Delafossites: Synthesis and Stability Aspects. *Chem. Mater.* **2013**, *25*, 4423–4435. [\[CrossRef\]](#)
34. Ma, B.; Zhu, M.; Zheng, M.; Hou, Y. Improvement in electrical properties of thermoelectric CuAlO₂ ceramics aided by aluminosilicate glass. *Int. J. Appl. Ceram. Technol.* **2018**, *15*, 1301–1309. [\[CrossRef\]](#)
35. Mudenda, S.; Kale, G.M.; Hara, Y.R.S. Rapid synthesis and electrical transition in p-type delafossite CuAlO₂. *J. Mater. Chem. C* **2014**, *2*, 9233–9239. [\[CrossRef\]](#)

36. Thu, T.V.; Thanh, P.D.; Suekuni, K.; Hai, N.H.; Mott, D.; Koyano, M.; Maenosono, S. Synthesis of delafossite CuAlO_2 p-type semiconductor with a nanoparticle-based Cu(I) acetate-loaded boehmite precursor. *Mater. Res. Bull.* **2011**, *46*, 1819–1827. [[CrossRef](#)]
37. Vojislavljević, K.; Malič, B.; Senna, M.; Drnovšek, S.; Kosec, M. Solid state synthesis of nano-boehmite-derived CuAlO_2 powder and processing of the ceramics. *J. Eur. Ceram. Soc.* **2013**, *33*, 3231–3241. [[CrossRef](#)]
38. Armelao, L.; Barreca, D.; Bertapelle, M.; Bottaro, G.; Sada, C.; Tondello, E. A sol–gel approach to nanophasic copper oxide thin films. *Thin Solid Film.* **2003**, *442*, 48–52. [[CrossRef](#)]
39. Das, B.; Renaud, A.; Volosin, A.M.; Yu, L.; Newman, N.; Seo, D.-K. Nanoporous Delafossite CuAlO_2 from Inorganic/Polymer Double Gels: A Desirable High-Surface-Area p-Type Transparent Electrode Material. *Inorg. Chem.* **2015**, *54*, 1100–1108. [[CrossRef](#)]
40. Ishiguro, T.; Kitazawa, A.; Mizutani, N.; Kato, M. Single-crystal growth and crystal structure refinement of CuAlO_2 . *J. Solid State Chem.* **1981**, *40*, 170–174. [[CrossRef](#)]
41. Shannon, R.D.; Rogers, D.B.; Prewitt, C.T.; Gillson, J.L. Chemistry of noble metal oxides. III. Electrical transport properties and crystal chemistry of ABO_2 compounds with the delafossite structure. *Inorg. Chem.* **1971**, *10*, 723–727. [[CrossRef](#)]
42. Benko, F.A.; Koffyberg, F.P. Opto-electronic properties of CuAlO_2 . *J. Phys. Chem. Solids* **1984**, *45*, 57–59. [[CrossRef](#)]
43. Ghosh, C.K.; Popuri, S.R.; Mahesh, T.U.; Chattopadhyay, K.K. Preparation of nanocrystalline CuAlO_2 through sol–gel route. *J. Sol-Gel Sci. Technol.* **2009**, *52*, 75–81. [[CrossRef](#)]
44. Jiang, H.F.; Zhu, X.B.; Lei, H.C.; Li, G.; Yang, Z.R.; Song, W.H.; Dai, J.M.; Sun, Y.P.; Fu, Y.K. Effect of Cr doping on the optical–electrical property of CuAlO_2 thin films derived by chemical solution deposition. *Thin Solid Film.* **2011**, *519*, 2559–2563. [[CrossRef](#)]
45. Li, G.; Zhu, X.; Lei, H.; Jiang, H.; Song, W.; Yang, Z.; Dai, J.; Sun, Y.; Pan, X.; Dai, S. Preparation and characterization of CuAlO_2 transparent thin films prepared by chemical solution deposition method. *J. Sol-Gel Sci. Technol.* **2010**, *53*, 641–646. [[CrossRef](#)]
46. Ghahari, S.; Ghafari, E.; Assi, L. Pore structure of cementitious material enhanced by graphitic nanomaterial: A critical review. *Front. Struct. Civ. Eng.* **2018**, *12*, 137–147. [[CrossRef](#)]
47. Lee, M.S.; Kim, T.Y.; Kim, D. Anisotropic electrical conductivity of delafossite-type CuAlO_2 laminar crystal. *Appl. Phys. Lett.* **2001**, *79*, 2028–2030. [[CrossRef](#)]